Supplementary Information

Syringe injectable electronics

Jia Liu, Tian-Ming Fu, Zengguang Cheng, Guosong Hong, Tao Zhou, Lihua Jin, Madhavi Duvvuri, Zhe Jiang, Peter Kruskal, Chong Xie, Zhigang Suo, Ying Fang, Charles M. Lieber*

*Corresponding author. E-mail: cml@cmliris.harvard.edu

This file includes:

Supplementary Materials and Methods
Supplementary References
Supplementary Table 1
Supplementary Figures 1-13

Materials and Methods

1. Mesh and control structure designs

1.1 Open mesh electronics

The overall structure and relevant parameters of the macroporous mesh electronics are illustrated in Supplementary Fig. 1. The key design and fabrication parameters are as follows: W, the total mesh width; w_1, width of longitudinal ribbons along injection/long axis of mesh, w_2, width of transverse ribbons, that cross and connect to the longitudinal ribbons with an angle, α, relative to the longitudinal ribbons; L_1, the mesh unit cell length in the longitudinal direction; L_2, the mesh unit cell length in the transverse direction; and w_m, the width of metal lines, which run along the longitudinal ribbons. The longitudinal and transverse ribbon widths ranged from 5-40 μm, and α was 45 or 0°. The embedded metal (SU-8/metal/SU-8) interconnects run along longitudinal ribbons; the metal contacts to nanowire transistor and bend-up passive metal sensors also have a metal line component embedded in the transverse ribbons. The specific parameters for injectable mesh electronics designs used in our studies are summarized as sample #1-6 in Supplementary Table 1.

1.2 Thin film electronics

Control samples with the same thickness as the mesh electronics but comprising a standard flexible thin-film structure were also designed and fabricated. The metal line patterns, thickness and widths are the same as design #1 of tilted mesh electronics (Supplementary Table 1). The overall widths, W, of thin film electronics were 0.1-5 mm. The parameters of the thin film electronics designs used in our studies are summarized as samples #7 and 8 in Supplementary Table 1.

2. Free-standing mesh electronics fabrication

2.1 Initial fabrication steps

The overall fabrication of the syringe injectable electronics is based on methods described previously[1, 2]. Key steps (Supplementary Fig. 2) are as follows: (1) 100 nm nickel metal, which serves as a final relief layer, was deposited on the silicon fabrication substrate (600 nm SiO_2, n-type 0.005 Ω·cm, Nova Electronic Materials, Flower Mound, TX) by thermal evaporation; (2) A 300 to 400 nm layer of SU-8 photoresist (2000.5; MicroChem Corp., Newton, MA) was spin-coated on the fabrication substrate, prebaked (65 °C/2 min; 95 °C/2 min), and then (3) patterned by photolithography to define the bottom SU-8 layer of the injectable mesh electronics structure. (4) After post baking (65 °C/2 min; 95 °C/2 min), and developing by SU-8 Developer (MicroChem Corp., Newton, MA), the SU-8 pattern was cured at 180 °C for 20 min. At this point, either of two distinct types of device elements, silicon nanowire transistors or passive metal electrodes, was integrated in the fabrication process; these are described separately, followed by common steps used to complete fabrication of the free-standing mesh electronics.

2.2 Nanowire transistor elements

(5a) A 300 to 400 nm layer of SU-8 photoresist was deposited on the fabrication substrate, prebaked (65 °C/2 min; 95 °C/4 min), and then (5b) silicon nanowires[3] were aligned on the SU-8 layer by contact printing as described previously[4]. (5c) Photolithography was used to define the

nanowire device regions, and after post-baking (65 °C/2 min; 95 °C/2 min), the pattern was developed by SU-8 Developer washed with isopropanol (2 times, 30 s per wash) to remove nanowires outside of the device regions. (5d) The new SU-8 pattern was cured at 180 °C/20 min. (5e) Nanowire device element contacts were fabricated as described previously[2, 5]. Briefly, the substrate was coated with 300 nm LOR 3A and 500 nm S1805 (MicroChem Corp., Newton, MA) double layer resist and patterned by photolithography. Sequential Cr/Pd/Cr (1.5/50–80/1.5 nm) metal layers were deposited by thermal evaporation followed by metal lift-off in Remover PG (MicroChem Corp., Newton, MA) to define the minimally-stressed nanowire contacts.

2.3 Metal electrode elements

(6a) The substrate was spin-coated with LOR 3A and S1805 double layer resist with similar thicknesses as described above. (6b) 20 μm diameter sensor pads (Cr/Pt, 5/50 nm) were defined by photolithography and electron beam evaporation followed by metal lift-off in Remover PG. (6c) The substrate was then spin-coated with LOR 3A and S1805 double layer resist with similar thicknesses as described above again. (6d) For sensors designed to bend-out from the mesh plane, nonsymmetrical Cr/Pd/Cr (1.5/50-80/30-50 nm) metal lines (200 μm long) were patterned by photolithography and subsequent thermal deposition followed by metal lift-off in Remover PG.

2.4 Completion of free-standing mesh electronics fabrication

(7) The substrate was coated with LOR 3A and S1805 double layer resist with similar thicknesses as described above and patterned by photolithography. Unstressed, symmetrical Cr/Au/Cr (1.5/50–100/1.5 nm) metal lines were sequentially deposited followed by metal lift-off in Remover PG to define the minimally stressed interconnects/address lines[2, 5]. All metal lines were defined such that they are on top of and smaller in width than the SU-8 mesh pattern described in steps 1-5. (8) A 300 to 400 nm layer of SU-8 photoresist was deposited on the fabrication substrate, pre-baked (65 °C/2 min; 95 °C/2 min), and then patterned by photolithography to match the lower SU-8 mesh structure and serve as top encapsulating/passivating layer of the metal contacts/interconnects (except for active device regions). The structure was post-baked, developed, and cured as described above. (9) In the case of nanowire transistor devices, 300 and 500 nm thick layers of LOR 3A and S1805 photoresist were deposited and defined by photolithography to protect the device region during release of the mesh from the fabrication substrate. (10) The syringe injectable mesh electronics were released from the substrate by etching the nickel layer (40% $FeCl_3$:39% HCl:H_2O = 1:1:20) for 3 - 4 hours at 25 °C and then transferred to deionized (DI) water by glass pipette (5 mL, Disposable Pasteur Pipets, Lime Glass, VWR International, LLC, Radnor, PA). (12) The photoresist protection was removed from nanowire device meshes by exposure to ultraviolet light (430 nm, 120 s) and immersion in developer solution (MF-CD-26, MicroChem Corp., Newton, MA)[6].

3. Injection of electronics

3.1 Surface modification of mesh electronics for aqueous injection

Freestanding mesh electronics structures were transferred by glass pipette sequentially to (a) DI water for 5 min., (b) aqueous poly-D-lysine (PDL, 0.5-1.0 mg/ml, MW 70,000-150,000, Sigma-Aldrich Corp., St. Louis, MO) solution for 2-12 hours at 25 °C, and (c) 1x Phosphate Buffered

Saline (PBS) (HyClone™ Phosphate Buffered Saline, Thermo Fisher Scientific Inc., Pittsburgh, PA) at 25 °C for storage (time limited for storage: 1-2 days).

3.2 Glass needles for injection and imaging

Glass needles for injection and imaging were prepared by using a commercial pipette puller (Model P-97, Sutter Instrument, CA). To prepare channels for imaging, the pulling was halted and suspended in the middle without breaking the glass tube. The channel sizes were characterized by confocal fluorescence microscopy, where rodamine-6G (Sigma-Aldrich Corp., St. Louis, MO) solution was filled into the channel for imaging. For a channel inner diameter (ID) smaller than 300 μm, epoxy glue was used to increase stability during imaging. Clean-cut needles were prepared by scoring (#CTS, Sutter Instrument, CA) and mechanical breakage followed by optical microscopy examination.

To introduce the mesh electronics into glass needles, the tip end of a glass needle was connected to a syringe, and then the large end of the glass needle was used to suck the mesh electronics in towards the sharp needle tip. The correct orientation of the mesh electronics (i.e., recording devices at the needle tip) is readily achieved given visual asymmetry of the structures (see Supplementary Fig. 3a). The glass needle was removed from the plastic tube/syringe and the large end (Supplementary Fig. 3b) connected to a conventional micropipette holder (Q series holder, Harvard Apparatus, Holliston, MA). A microinjector was connected to this holder by plastic tubing. The injection process was controlled using a microinjector (NPIPDES, ALA Scientific instruments Inc., Farmingdale, NY); for example, the injection length per microinjector pulse can yield well-defined ejection of the mesh electronics from the needles (Supplementary Fig. 3c).

3.3 Injection through metal needles

After surface modification, the mesh electronics was transferred by glass pipette into a syringe (Pressure Control Glass Syringes, Cadence, Inc., Cranston, RI) fitted with a metal needle (18-32 gauge, Veterinary Needles, Cadence, Inc., Cranston, RI). The syringe was assembled and the plunger carefully pressed to drive the region containing devices into the needle, and then to inject the mesh into aqueous solutions (Supplementary Fig. 4c).

3.4 Input/output (I/O) bonding with anisotropic conductive film (ACF)

The I/O connection pads at the end of the mesh electronics structure (Supplementary Fig. 1) were bonded to a flexible cable post-injection for measurements. First, the I/O region was allowed to unfold in solution layer outside of the injected materials, and then rinsed with ethanol and dried. Second, a piece of ACF (ACF, CP-13341-18AA, Dexerials America Corporation, San Jose, CA), 1.5 mm wide and 15 mm long was over the I/O pads and partially bonded for 10 sec at 75 ºC and 1 MPa using a homemade or commercial bonder (Fineplacer Lambda Manual Sub-Micron Flip-Chip Bonder, Finetech, Inc., Manchester, NH). Third, a flexible cable (FFC/FPC Jumper Cables PREMO-FLEX, Molex, Lisle, IL) was placed on the ACF, aligned with I/O pads and bonded for 1-2 min at 165-200 ºC and 4 MPa (Supplementary Figs. 5a, b).

3.5 Injection of mesh electronics

3.5.1 Co-injection into polymer cavities with a polymer precursor

Cavities for injection (Supplementary Fig. 8a) were formed from two pieces of cured polydimethylsiloxane (PDMS, Sylgard 184, Dow Corning Corporation, Midland, MI). The PDMS cavity was designed with a step-like internal corrugation (4 steps, 0.1 cm drop/step, and projected cavity area of 2 x 4.8 cm^2). Key steps for the co-injection are as follows: (1) mesh electronics were transferred from DI water to ethanol after etching. (2) PDMS pre-polymer components were prepared in a 10:1 (base: cure agent; Sylgard 184, Dow Corning Corporation, Midland, MI), diluted by hexane 1:3 PDMS:hexane volume ratio, and then (3) the mesh electronics was transferred to the PDMS/hexane solution and the resulting homogeneous suspension loaded into a glass syringe. (4) The device region of mesh was injected through a 16 or 18 gauge metal needle into the cavity (Supplementary Fig. 8b), and the I/O region was positioned outside the cavity on a silicon wafer or glass slide. (5) The I/O region was washed with hexane to remove PDMS residue and bonded to a flexible cable interface as described above. The PDMS cavity with the mesh electronics was left at room temperature for 2-4 hours to allow for evaporation of hexane, and then undiluted PDMS precursors were injected into the cavity to fill the entire volume and cured at room temperature for 48 h.

3.5.2 Injection into Matrigel™

PDL modified mesh electronics were transferred to 1x PBS solution, autoclaved for 1 hour, transferred into Neurobasal™ medium (Invitrogen, Grand Island, NY) by glass pipette, and then loaded into glass syringe as described above. 100% Matrigel™ (BD Bioscience, Bedford, MA) alone or diluted with Neurobasal™ medium to 75 and 25% (v/v) was polymerized for 20 min at 37 ºC in an incubator. Mesh electronics were injected into the 100, 75 and 25% polymerized Matrigel™ samples, and the hybrid structures were incubated at 37 ºC and imaged (Figs. 3d – 3f) at different times to investigate mesh unfolding in the gel.

3.5.3 Co-injection of mesh electronics with neurons

Hippocampal neurons (Gelantis, San Diego, CA) were prepared using a standard protocol described previously[1]. In brief, 5 mg of NeuroPapain Enzyme (Gelantis, San Diego, CA) was added to 1.5 ml of NeuroPrep Medium (Gelantis, San Diego, CA). The solution was kept at 37 ºC for 15 min, and sterilized with a 0.2 μm syringe filter (Pall Corporation, MI). Day 18 embryonic Sprague/Dawley rat hippocampal tissue with shipping medium (E18 Primary Rat Hippocampal Cells, Gelantis, San Diego, CA) was spun down at 200 g for 1 min. The shipping medium was exchanged for NeuroPapain Enzyme medium. A tube containing tissue and the digestion medium was kept at 30 ºC for 30 min and manually swirled every 2 min, the cells were spun down at 200 g for 1 min, the NeuroPapain medium was removed, and 1 ml of shipping medium was added. After trituration, cells were isolated by centrifugation at 200 g for 1 min, and then resuspended in 5-10 mg/ml Matrigel™ at 4 ºC. Matrigel™ with neurons were mixed with electronics at 4 ºC and then loaded into syringe with metal gauge needle. The electronics and neurons were co-injected into 30% (v/v) polymerized Matrigel™ in culture plate and then placed in incubator to allow Matrigel™ to gel at 37 ºC for 20 min. Then 1.5 ml of NeuroPure plating medium was added. After 1 day, the plating medium was changed to Neurobasal™ medium (Invitrogen, Grand Island, NY) supplemented with B27 (B27 Serum-Free Supplement, Invitrogen, Grand Island, NY), Glutamax™ (Invitrogen, Grand Island, NY) and 0.1%

Gentamicin reagent solution (Invitrogen, Grand Island, NY). The *in-vitro* co-cultures were maintained at 37 °C with 5% CO_2 for 14 days, with medium changed every 4-6 days. After incubation, cells were fixed with 4% paraformaldehyde (Electron Microscope Sciences, Hatfield, PA) in PBS for 15-30 min, followed by 2-3 washes with ice-cold PBS. Cells were pre-blocked and permeabilized (0.2-0.25% Triton X-100 and 10% feral bovine serum (F2442, Sigma-Aldrich Corp. St. Louis, MO) for 1 hour at room temperature. Next, the cells were incubated with primary antibodies Anti-neuron specific β-tubulin (in 1% FBS in 1% (v/v)) for 1 hour at room temperature or overnight at 4 ºC. Then cells were incubated with the secondary antibodies AlexaFluor-546 goat anti-mouse IgG (1:1000, Invitrogen, Grand Island, NY).

3.6 *In vivo* rodent brain injection

3.6.1 Mouse preparation

(1) Adult (25-35 g) male C57BL/6J mice (Jackson lab) and Adult (25-35 g) male transgenic mice FVB/N-Tg (GFAPGFP)14Mes/J (Jackson lab) were group-housed, given access to food pellets and water *ad libitum* and maintained on a 12 h: 12 h light: dark cycle. (2) All animals were held in a facility beside lab 1 week prior to surgery, post-surgery and throughout the duration of the behavioral assays to minimize stress from transportation and disruption from foot traffic. All procedures were approved by the Animal Care and Use Committee of Harvard University and conformed to US National Institutes of Health guidelines.

3.6.2 Stereotaxic surgery

(3) After animals were acclimatized to the holding facility for more than 1 week, they were anesthetized with a mixture of 60 mg/kg of ketamine and 0.5 mg/kg medetomidine (Patterson Veterinary Supply Inc., Chicago, IL) administered intraperitoneal injection, with 30 μL update injections of ketamine to maintain anesthesia during surgery. A heating pad (at 37 °C) was placed underneath the body to provide warmth during surgery. Depth of anesthesia was monitored by pinching the animal's feet periodically. (4) Animals were placed in a stereotaxic frame (Lab Standard Stereotaxic Instrument, Stoelting Co., Wood Dale, IL) and then (5) a 1 mm longitudinal incision was made, and the skin was resected from the center axis of the skull, exposing a 2 mm by 2 mm portion of the skull. (6) A 0.5 mm diameter hole was drilled into the frontal and parietal skull plates using a dental drill (Micromotor with On/Off Pedal 110/220, Grobet USA, Carlstadt, NJ). (7) The dura was incised and resected. Sterile 1x PBS was swabbed on the brain surface to keep it moist throughout the surgery. A stereotaxic arm was used to hold and position the needle containing the injectable mesh electronics.

3.6.3 Stereotaxic injection

(8) Mesh electronics were autoclaved for 1 hour in 1x PBS solution before injection, and then transferred into Neurobasal™ medium and loaded into the autoclaved glass needle as described above. (9) The glass needle (with diameter of 100-200 μm) was mounted to a micropipette setup for injection. (10) The needle was lowered into the exposed brain surface approximately 1-2 mm into the skull (Interaural: 6.16 mm, Bregma: -3.84 mm) to test the effects of deep brain and superficial layer injections. A syringe or microinjector was used to inject the mesh electronics into the brain. The needle was retracted during injection using a linear translational stage on the stereotaxic frame. The mesh is injected concomitantly with retraction of the needle so that the

electronics is extended in the longitudinal (injection) direction. For targeting cortex/hippocampus region and lateral ventricle, sample #4 and #5 in Supplementary Table 1 were used, respectively. (11) After injection, the needle was withdrawn from the brain tissue and the I/O region was ejected on the surface of the skull and recording scaffold.

3.6.4 Acute recording

(12) A ceramic plate/scaffold with a 0.5-1 cm diameter hole was fixed above the mouse brain, and (13) silicone elastomer (World Precision Instruments Inc., Sarasota, FL) was used to seal the gap between the mouse skull and the scaffold to form a chamber that was kept filled with 1x PBS solution. (14) After injection of electronics as described in steps 10-11, the I/O region of electronics was unfolded on the surface of the ceramic scaffold. (15) I/O pads were bonded to a flexible cable by ACF as described above. (16) A 32-channel Intan RHD 2132 amplifier evaluation system (Intan Technologies LLC., Los Angeles, CA) was used for acute electrophysiology recording with an Ag/AgCl electrode acting as the reference. A 20 kHz sampling rate and 60 Hz notch were used during acute recording. A 300-6000 Hz band-pass filter was applied to original recording data for single-unit spikes analyses. Superposition of single-unit spikes was conducted by Clampfit (Molecular Devices, Sunnyvale, CA).

3.6.5 Chronic testing

(17) After injection, the skin that was retracted from the center axis was replaced and the incision was sealed with C&B-METABOND (Cement System, Parkell, Inc., Edgewood, NY). (18) Anti-inflammatory and anti-bacterial ointment was swabbed onto the skin after surgery. A 0.3 mL intraperitoneal injection of Buprenex (Patterson Veterinary Supply Inc. Chicago, IL, diluted with 0.5 ml of PBS) was administered at 0.1 mg/kg to reduce post-operative pain. (19) Animals were observed for 4 hours after surgery and hydrogel was provided for food, and heating pad was on at 37 °C for the remainder of post-operative care. All procedures complied with the United States Department of Agriculture guidelines for the care and use of laboratory animals and were approved by the Harvard University Office for Animal Welfare.

3.6.6 Incubation and behavioral analysis

(20) Animals were cared every day for 3 days after the surgery and every other day after the first 3 days. (21) Animals were administered 0.3 mL of Buprenex (0.1 mg/kg, diluted with 0.5 mL 1x PBS) every 12 hours for 3 days. Animals were also observed every other day for behavioral changes. Animals, which were surgically operated on, were housed individually in cages with food and water ad libitum. The room was maintained at constant temperature on a 12-12 h light-dark cycle.

3.6.7 Brain tissue preparation for chronic immunostaining

Key steps for brain tissue immunostaining are as follows: (1) 4-5 weeks after the surgery, mice underwent transcardial perfusion (40 mL 1x PBS) and were fixed with 4% formaldehyde (Sigma-Aldrich Corp., St. Louis, MO, 40 mL)[7]. (2) Mice were decapitated and brains were removed from the skull and set in 4% formaldehyde for 24 hours as post fixation and then 1x PBS for 24 hours to remove excess formaldehyde. The mesh electronics remained inside the brain throughout fixing process. (3a) For samples with mesh electronics injected in the cortex/hippocampus region, brains were blocked, separated into the two hemispheres, and (3b) mounted on the vibratome stage (Vibrating Blade Microtome Leica VT1000 S, Leica

Microsystems Inc. Buffalo Grove, IL). (3c) 50-100 μm thick vibratome tissue slices (horizontal and coronal orientations) were prepared for staining. (4a) For samples with mesh electronics injected in lateral ventricle, brains were blocked and then fixed in 1% (w/v) agarose type I-B (Sigma-Aldrich Corp., St. Louis, MO) to fix the position of mesh electronics in the lateral ventricle cavity and then (4b) mounted on the vibratome stage. (4c) 100 μm thick vibratome tissue slices (horizontal orientations) were prepared. Coronal slices allowed for cutting in a direction along the long axis of the injection on the frontal plane and horizontal slices allowed for cuts in a direction perpendicular to the long axis of injection. (5a) Sample prepared for cryosectioning were transferred to sucrose solution (30%) overnight, and then (5b) transferred to Cryo-OCT compound (VWR, International, LLC, Chicago, IL) with frozen at -80 °C. (5c) Frozen samples were mounted on the stage of a Leica CM1950 cryosectioning instrument (Leica Microsystems Inc., Buffalo Grove, IL) and sectioned into 10 μm thick horizontal slice.

3.6.8 Immunostaining

(6) Slices >30 μm thick were then cleared with 5 mg/mL sodium borohydride in HEPES-buffered Hanks saline (HBHS, Invitrogen, Grand Island, NY) for 30 minutes, with 3-times following HBHS washes at 5-10 minute intervals. Sodium azide (4%) diluted 100x in HBHS was included in all steps. (7) Slices were incubated with 0.5% (v/v) Triton X-100 in HBHS for 30 min at room temperature. (8) All slices were blocked with 5% (w/v) FBS and incubated overnight at room temperature. (9) Slices were washed four times, 30 min intervals, with HBHS to clear any remaining serum in the tissue. (10) Slices were then incubated overnight at room temperature with the glial fibrillary acidic protein (GFAP) primary antibody (targeting astrocytes, 1:1000, #13-0300 Invitrogen, Grand Island, NY) and/or NeuN primary antibody (targeting nuclei of neurons, 1:200, #ab77315 AbCam, Cambridge, MA) containing 0.2% triton and 3% serum. (11) After incubation, slices were washed 4-times for 30 min with HBHS. Slices were incubated with secondary antibody (1:200; Alexa Flour® 546 goat anti-rat secondary antibody, 1:200, Alexa Fluor® 488 goat anti-rabbit secondary antibody and/or 1:200, Alexa Fluor® 647 goat anti-chicken secondary antibody (for GFP labeled mice), Invitrogen, Carlsbad, CA) and counterstained with Hoechst 33342 (nuclein stain 1:150, #46C3-4, Invitrogen , Carlsbad, CA) with 0.2% Triton and 3% serum overnight. (12) After the final washes (4-times, 30 min each with HBHS), slices were mounted on glass slides with coverslips using Prolong Gold (Invitrogen, Carlsbad, CA) mounting media. The slides remained covered (protected from light) at room temperature, allowing for 12 hours of clearance before imaging. When the antibody solutions were first prepared, they included 0.3 Triton X-100 and 5% FBS.

4. Characterization

4.1 Structure characterization

Scanning electron microscopy (SEM, Zeiss Ultra55/Supra55VP field-emission SEMs) was used to characterize the mesh electronics structures. Confocal, bright-field and epi-fluorescence imaging was carried out using an Olympus Fluoview FV1000 confocal laser scanning microscope or Zeiss LSM 780 confocal microscope (Carl Zeiss Microscopy, Thornwood, NY). Confocal images were acquired using 405, 473 and 559 nm wavelength lasers to excite components labeled with Hoechst 33342, Alexa Flour® 488, Alexa Flour® 546, GFP, and Rodamine-6G fluorescent dyes. A 635 nm wavelength laser was used for imaging Alexa Flour® 647, and imaging metal interconnects in reflective mode. Epi-fluorescence images were acquired

using a mercury lamp together with standard DAPI (EX:377/50,EM:447/60), GFP (EX:473/31,EM520/35) and TRITC (EX:525/40,EM:585/40) filters. *ImageJ* (ver. 1.45i, Wayne Rasband, National Institutes of Health, USA) was used for 3D reconstruction and statistical analysis of the confocal images, and overlapping epi-fluorescence images and bright-field images. Matlab was used for statistical analysis of fluorescence intensity of the confocal images for immunostained tissue slices.

4.2 Imaging of mesh electronics in glass channels

Mesh electronics and thin film control samples with different width and structure (sample #1-3, 7-8 in Supplementary Table 1) were injected into the glass channels following the same injection process described above except that process was stopped so that the mesh remained in part in the constriction of the 'needle'. Confocal fluorescence microscopy was used to image the 3D structure of mesh electronics and thin films in different diameter glass needles. 3D reconstructed images were obtained using *Image J*. Cross-section images of the samples were obtained using *ImageJ* to re-slice 3D reconstructed images in transverse direction with 1 μm steps along the longitudinal direction.

4.3 Micro-computed tomography

Structures of injected mesh electronics cured in PDMS and Matrigel™ were imaged using a HMXST Micro-CT X-ray scanning system with a standard horizontal imaging axis cabinet (model: HMXST225, Nikon Metrology, Inc., Brighton, MI). Typical imaging parameters for electronics in PDMS were 75 kV acceleration voltage and 120 μA electron beam current; for electronics in Matrigel™, 80 kV acceleration voltage and 130 μA electron beam current were used. In both cases, shading correction and bad pixel correction were applied before scanning to adjust the X-ray detector; no filter was applied. *CT Pro* (ver. 2.0, Nikon-Metris, UK) was used to calibrate centers of Micro-CT images. *VGStudio MAX* (ver. 2.0, Volume Graphics GMbh, Germany) was used for 3D reconstruction and analysis of the calibrated Micro-CT images.

4.4 Electrical measurements

4.4.1 Yield of injection

The yield of working devices after injection was determined by measuring the impedance of passive metal electrodes and conductance of nanowire devices before and after injection as follows: (1) As-made 2D mesh electronics were partially immersed in etchant solution as described above to release only the I/O region of mesh electronics and then mesh electronics was transferred to DI water and then dried in ethanol, while the released I/O region was unfolded on the substrate. (2) Next, the remaining nickel layer was etched and the sample transferred to DI water and dried in ethanol such that the device region was unfolded on the substrate. This two-step etching process allows the mesh electronics to fully unfold on the substrate in a manner that it can be subsequently re-suspended for injection. (3) Mesh electronics were modified by PDL as described above. (4a) For passive electrodes, the impedance (Z_0) at 1 kHz, and impedance-frequency (*Z-f*) data were recorded in 1x PBS using an Agilent B1500A semiconductor device parameter analyzer (Agilent Technologies Inc., Santa Clara, CA) with B1520A-FG multi-frequency capacitance measurement unit (Agilent Technologies Inc., Santa Clara, CA). Electrodes with impedance at 1 kHz below 1.5 MΩ were taken as suitable passive metal electrodes with total number, N_0. (4b) For nanowire devices, the conductance (G_0) for each

device was measured using a probe station (Lake Shore Cryotronics, Inc., Westerville, OH). Current-voltage (*I-V*) data were recorded using an Agilent 4156C semiconductor parameter analyzer (Agilent Technologies Inc., Santa Clara, CA) with contacts to device through probe station. Devices with conductance above 100 nS were taken as suitable nanowire devices with total number, N_0. (5) After impedance/conductance measurements, mesh electronics were immersed in DI water for 4 - 6 hours to suspend them, (6) mesh samples were transferred by glass pipette to PDL aqueous solution for surface modification as described above, and then (7) loaded into syringes fitted with ID needles from 100 to 600 μm and into a chamber with I/O unfolded on a substrate adjacent to the chamber. (8) Ethanol was used to rinse and dry the I/O. (9a) The impedance (Z_1) of the passive electrodes was measured as in step 4a, and the total number of electrodes meeting above criteria, N_1, post-injection was recorded. Yield and impedance changes in Fig. 1H were calculated as N_1/N_0 and $(Z_1-Z_0)/Z_0$, respectively. (9b) The conductance (G_1) of nanowire devices was measured again, and the total number, N_1, meeting the above criteria (step 4b above) was determined. Yield and conductance changes in Fig. 1I were calculated as N_1/N_0 and $(G_1-G_0)/G_0$, respectively. All measurements have been repeated for 16 different devices.

4.4.2 Test of ACF bonding

The connection resistance of ACF was measured to investigate the influence of bonding on electrical properties of devices (Supplementary Figs. 5e and 5f). The conductance of each device (connected metal wires) was measured by probe station as R_0 and R_1 before and after ACF bonding, respectively. The connection resistance for each I/O pad (100 μm diameter) was calculated as $(R_1-R_0)/2$, illustrated in Supplementary Fig. 5e. The calculated connection resistance after ACF bonding with commercial (ca. 21.2 Ω) and homemade (ca. 33.7 Ω) instruments (Supplementary Fig. 4d), was <0.05% of the typical nanowire resistance and <0.01% of the typical metal electrode impedance at 1 kHz. The insulation resistance between I/O pads without circuits was over 10 GΩ. These measurements and analyses demonstrate that ACF bonding had little influence on electrical properties of injectable mesh electronics, which ensured reliable measurements with injectable mesh electronics devices in the applications described in the text. Comparison of the connection resistance values obtained using a standard flip-chip bonder and custom set-up suitable for bonding in restricted environments, including *in vivo* measurements, (Supplementary Fig. 5, e and f) shows similar values that are also comparable to reported contact resistances for ACF[8].

4.4.3 Piezoresistance measurements

The piezoresistance response of strained nanowire devices was measured as conductance change of device subject to the deformation of PDMS structure. In brief, the I/O pads were bonded to a flexible cable as described above, and connected to a multi-channel current/voltage preamplifier (Model 1211, DL Instruments, Brooktondale, NY), filtered with a 3 kHz low pass filter (CyberAmp 380, Molecular Devices, Sunnyvale, CA), and digitized at a 1 kHz sampling rate (AxonDigi1440A, Molecular Devices, Sunnyvale, CA), with a 100 mV DC source bias voltage. Pressure was applied along z-axis for 20 sec using a homemade linear translation stage.

4.4.4 SU-8 passivation characterization

The effectiveness of our SU-8 passivation was characterized following immersion in Neurobasal™ medium at 37 °C for 6 weeks using impedance-frequency (*Z-f*) measurement. A PDMS chamber 2 mm in longitudinal direction and 5 mm in transverse direction was positioned over the interconnect lines (without exposing the sensor electrodes), filled with 1x PBS solution, and then *Z-f* data were recorded using an Agilent B1500A semiconductor device parameter analyzer with B1520A-FG multi-frequency capacitance measurement unit. Significantly, impedance measurements from 1 to 10 kHz for 16 different SU-8 passivated metal interconnect lines showed average values above 10 GΩ. The large impedance demonstrates that there is no obvious leakage through our thin SU-8 polymer passivation. In addition, the impedance at 1 kHz of the SU-8 passivated region, ~30 GΩ, is 10^4-10^5 larger than the typical values for our Pt-metal sensors.

5. Structure analysis and mechanical simulations

5.1 Number of rolls of mesh electronics inside glass needles

The mesh electronics rolls up in a scroll-like structure when injected through a glass needle. Theoretically, the number of circumferential rolls, N_{rolls} can be calculated by dividing the total width, W, of the mesh with the perimeter of the tube, πD, with, D, the tube ID, as $N_{rolls}=W/\pi D$ with values of 3.5, 6.3, and 10.5 for Fig. 2, c to e, (**I**), (**II**) and (**III**), respectively. Experimentally, the number of circumferential rolls was estimated from the cross sections of 3D reconstructed confocal images as follows: First, we count the number of longitudinal ribbon (LR) features, K_{LR}, in images of the scroll structure. Second, the number of LRs from a half circumference roll can be estimated as $n_{LR}= \pi D/2s$, where s is the distance between LRs. Finally, the total number of circumference rolls is $N'_{rolls} =2sK_{LR}/\pi D$, Using this method, the numbers of circumference rolls in Fig. 2, c to e are 3.4 ± 0.2, 6.0 ± 0.4 and 9.5 ± 1.0 for (**I**), (**II**) and (**III**), respectively. The uncertainty arises from the identification of longitudinal elements from 8 random cross-sections for each case; small deviations from geometric analysis above may be arise in part from a failure to count some longitudinal elements due to low fluorescence intensity.

5.2 Mechanical simulation

5.2.1 Bending stiffness simulation

We estimate the bending stiffness of the mesh electronics with different structures by finite element software ABAQUS. A unit cell is used for the simulation, where the tilt angle α is defined in Fig. 1D and mesh electronics are modeled with shell elements: A homogeneous single shell section with 700 nm thick SU-8 is assigned to the transverse ribbons; a composite section with three layers of 350 nm thick SU-8, 100 nm thick gold and another 350 nm thick SU-8 is assigned to the longitudinal ribbons. Both SU-8 and gold are modeled as linear elastic materials, with Young's modulus 2 Gpa and 79 GPa[9] respectively. To calculate the longitudinal and transverse bending stiffnesses, a fixed boundary condition is set at one of the ends parallel with the bending direction, and a small vertical displacement, d, is added at the other end. The external work, W, to bend the device is calculated. We define the effective bending stiffness of the device as the stiffness required of a homogenous beam to achieve the same external work W

under the displacement *d*. Therefore, the effective bending stiffness per width of the device can be estimated as[10]

$$D = \frac{2Wl^3}{3d^2b}$$

with *b* the width of the unit cell parallel with the bending direction, and *l* the length of the unit cell perpendicular to the bending direction (Supplementary Fig. 1b).

5.2.2 Effective bending stiffnesses of implantable probes.

The effective bending stiffness per width of the three-layer longitudinal ribbon, D_1, (longitudinal ribbon) in the mesh can be estimated as[10]

$$D_1 = \frac{E_s}{w_1}\left(\frac{h^3 w_1}{12} - \frac{h_m^3 w_m}{12}\right) + \frac{E_m}{w_1}\frac{h_m^3 w_m}{12}$$

where E_s is young's modulus of SU-8, E_m is young's modulus of gold, h is the total thickness of ribbon, h_m is the thickness of metal, w_1 is the total width of ribbon and w_m is the width of metal. When E_s = 2 GPa, E_m = 79 GPa[2], h = 800 nm, h_m = 100 nm, w_1 = 20 μm, w_m = 10 μm, D_1 = 0.086 nN·m.

The effective bending stiffness per width of standard silicon probes, D_2, can be estimated as [10]

$$D_2 = E_{silicon}\frac{h_{silicon}^3}{12}$$

where $E_{silicon}$ is the young's modulus of silicon, $h_{silicon}$ is the thickness of the probe. When $E_{silicon}$ = 165 GPa, $h_{silicon}$ = 15 μm[11], D_2 = 4.6 x 10^5 nN·m.

The effective bending stiffness per width of ultrasmall carbon electrodes, D_3, can be estimated as[10]

$$D_3 = E_{carbon}\frac{\pi d^3}{64}$$

Where E_{carbon} is the young's modulus of carbon fiber, d is the diameter of carbon fiber probe. When E_{carbon} = 234 GPa, d = 7 μm[7], D_3 = 3.9 x 10^4 nN·m.

The effective bending stiffness per width of planar shape probe, D_4, can be estimated as

$$D_4 = E_s\frac{h_s^3}{12}$$

Where E_s is the young's modulus of polyimide, h_s is the thickness of probe. When E_s = 2-2.73 GPa, h_s = 10-20 μm[12-14], D_4 = 0.16-1.3 x 10^4 nN·m.

5.2.3 Simulation of mesh electronics strain

The data in Fig. 1, Fig. 2 and Supplementary Fig. 4a and b show that mesh electronics can be injected in a rolled-up geometry through needles to 95 mm ID without breaking. We further quantified the importance of the rolled up geometry during injection by using simulations to estimate the strain distribution (Supplementary Fig. 7) versus needle ID the rolled-up geometry.

The simulation treats a unit cell of the mesh bent with a radius of curvature, R, where a fixed boundary condition sets the strain of one longitudinal ribbon at zero and the maximal principal strain, ε_m, value then occurs at the junction between the transverse and second longitudinal element of the unit cell (red dashed circle, inset, Supplementary Fig. 7). This strain value represents an upper limit given that other edge of the unit cell was set to zero for the simulation. The plot of this upper limit strain value versus $1/R$ (Supplementary Fig. 7) shows that strain increases linearly, where the black and red points/lines correspond to mesh electronics structural parameters summarized in Supplementary Table 1 (entries #2 and #5, respectively). The upper limit strain values extrapolated for a 100 μm ID needle for these two mesh structures, ca. 1.0%, are both smaller than the fracture strain, 5%, reported for a 20 μm thick SU-8 beam[15]. In addition, the stress intensity factor, K, for a thin film under pure bending exhibits a square root dependence on thickness[16], $K \sim E\varepsilon\sqrt{h}$, where E is the Young's modulus of the material, ε is the strain and h is the thickness of ribbon. The ε reaches the fracture strain of ribbon, ε_c, when K reaches the toughness of the material K_c. Since the thickness of SU-8 in our mesh structures is 700 nm (vs. 20 μm) the fracture strain of ribbon can be expected to be larger than 5%.

Supplementary References

1. Tian, B. *et al.* Macroporous nanowire nanoelectronic scaffolds for synthetic tissues. *Nature Mater.* **11**, 986-994 (2012).

2. Liu, J. *et al.* Multifunctional three-dimensional macroporous nanoelectronic networks for smart materials. *Proc. Natl. Acad. Sci. USA* **110**, 6694-6699 (2013).

3. Patolsky, F., Zheng, G. & Lieber C. M. Fabrication of silicon nanowire devices for ultrasensitive, label-free, real-time detection of biological and chemical species. *Nature Protoc.* **1**, 1711-1724 (2006).

4. Javey, A., Nam, S., Friedman, R. S., Yan, H. & Lieber, C. M. Layer-by-layer assembly of nanowires for three-dimensional, multifunctional electronics. *Nano Lett.* **7**, 773-777 (2007).

5. Tian, B. *et al.* Three-dimensional, flexible nanoscale field-effect transistors as localized bioprobes. *Science*, **329**, 831-834 (2010).

6. Qing, Q. *et al.* Free-standing kinked nanowire transistor probes for targeted intracellular recording in three dimensions. *Nature Nanotech*. **9**, 142-147 (2014).

7. Yoshida Kozai, T. D. *et al.* Ultrasmall implantable composite microelectrodes with bioactive surfaces for chronic neural interfaces. *Nature Mater.* **11**, 1065-1073 (2013).

8. Yim, M. & Paik, K. The contact resistance and reliability of anisotropically conductive film (ACF). *Advanced Packaging, IEEE Transactions on* **22**, 166-173 (1999).

9. http://www.microchem.com/pdf/SU-82000DataSheet2000_5thru2015Ver4.pdf

10. Steif, P. S. *Mechanics of Materials*, (Pearson, 2012).

11. Lee, H., Bellamkonda, R. V., Sun, W. & Levenston, M. E. Biomechanical analysis of silicon microelectrode-induced strain in the brain. *J. Neural Eng.* **2**, 81-89 (2005).

12. Kim, T. *et al.* Injectable, cellular-scale optoelectronics with applications for wireless optogenetics. *Science* **340**, 211-216 (2013).

13. Rousche, P. J. *et al.* Flexible polyimide-based intracortical electrode arrays with bioactive capability. *IEEE Trans. Biomed. Eng.* **48**, 361-371 (2001).

14. Navarro, X. *et al.* A critical review of interfaces with the peripheral nervous system for the control of neuroprostheses and hybrid bionic systems. *J. Peripher. Nerv. Syst.* **10**, 229-258 (2005).

15. Namazu, et al. Visco-elastic properties of micron-thick SU-8 polymers measured by two different types of uniaxial tensile tests. *MEMS 2005. 18th IEEE International Conference on*, 447-450 (2005).

16. Tada, H., Paris, P. C. & Irwin, G. R. in *Stress Analysis of Cracks Handbook.* 3rd edn, 55-57 (ASME Press, 2000).

Supplementary Table 1 Dimensions of mesh electronics. Samples #1-3 are mesh electronics used for imaging and injection experiments. Samples #4-5 are mesh electronics for *in vivo* experiment. Samples #6, and #7-8 are control rectangular mesh and flexible thin-film samples, respectively.

No.	W (mm)	w_1 (μm)	w_2 (μm)	L_1 (μm)	L_2 (μm)	w_m (μm)	α (°)
1	15	20	20	333	250	10	45
2	5	20	20	333	250	10	45
3	5	20	10	333	250	10	45
4	2	20	20	333	250	10	45
5	2	5	5	62.5	62.5	2	45
6	10	20	20	333	250	10	0
7	5	N/A	N/A	N/A	N/A	10	N/A
8	1.5	N/A	N/A	N/A	N/A	10	N/A

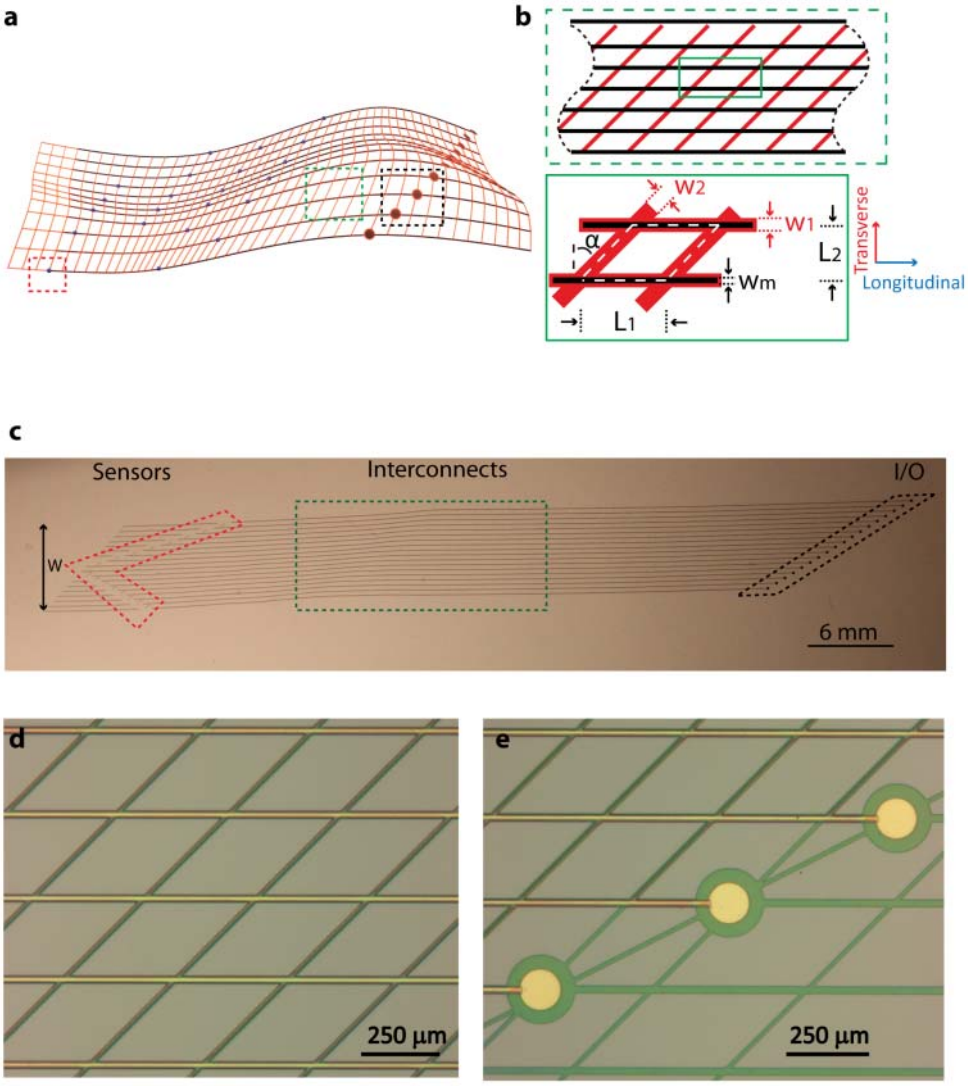

Supplementary Fig. 1. Structure of injectable electronics. **a**, Schematic of an injectable mesh electronics structure. The red-orange lines highlight the overall mesh structure and indicate the regions of supporting and passivating polymer mesh layers, the ca. horizontal black lines indicate metal interconnects between input/output (I/O) pads (black filled circles) and recording devices (blue filled circles). The red dashed box highlights two different types of devices - either electrochemical or field-effect transistors (FETs) (insets, Fig. 1, **i** and **j**), the green dashed box highlights mesh network metal interconnects, and the black dashed box highlights I/O pads. **b**, shows a schematic (upper panel) of the zoomed-in region of mesh network highlighted by green dashed box in **a**, where black horizontal lines correspond to metal interconnects, red-orange lines

highlight the transverse polymeric elements of the mesh. (Lower panel) corresponds to a single unit cell of the mesh (green box in upper panel) with the same color nomenclature as in (upper panel). The unit cell (white dashed lines) is defined by the following parameters: L_1 and L_2 are the unit lengths in the longitudinal and transverse directions, respectively; w_1 and w_2 are widths of the longitudinal and transverse mesh elements, respectively; and w_m is the width of metal interconnect lines. **c**, Optical image of an injectable mesh electronics structure unfolded on a glass substrate. W is the total width of the mesh electronics. The red dashed polygon highlights the position of metal or nanowire FET sensor devices (insets, Fig. 1, **i** and **j**). Metal interconnect lines (green dashed box) and metal I/O pads (black dashed box) are shown in detail in **d** and **e**, respectively. **d**, Bright field microscope image of the mesh structure (green dashed box in **c**) showing metal interconnects (horizontal, golden color lines), and polymer structural/passivation elements (greenish color lines). **e**, Bright field microscopy image from region of the black dashed box in **c** showing metal I/O pads (golden colored filled circles) supported by polymeric structural elements (greenish features).

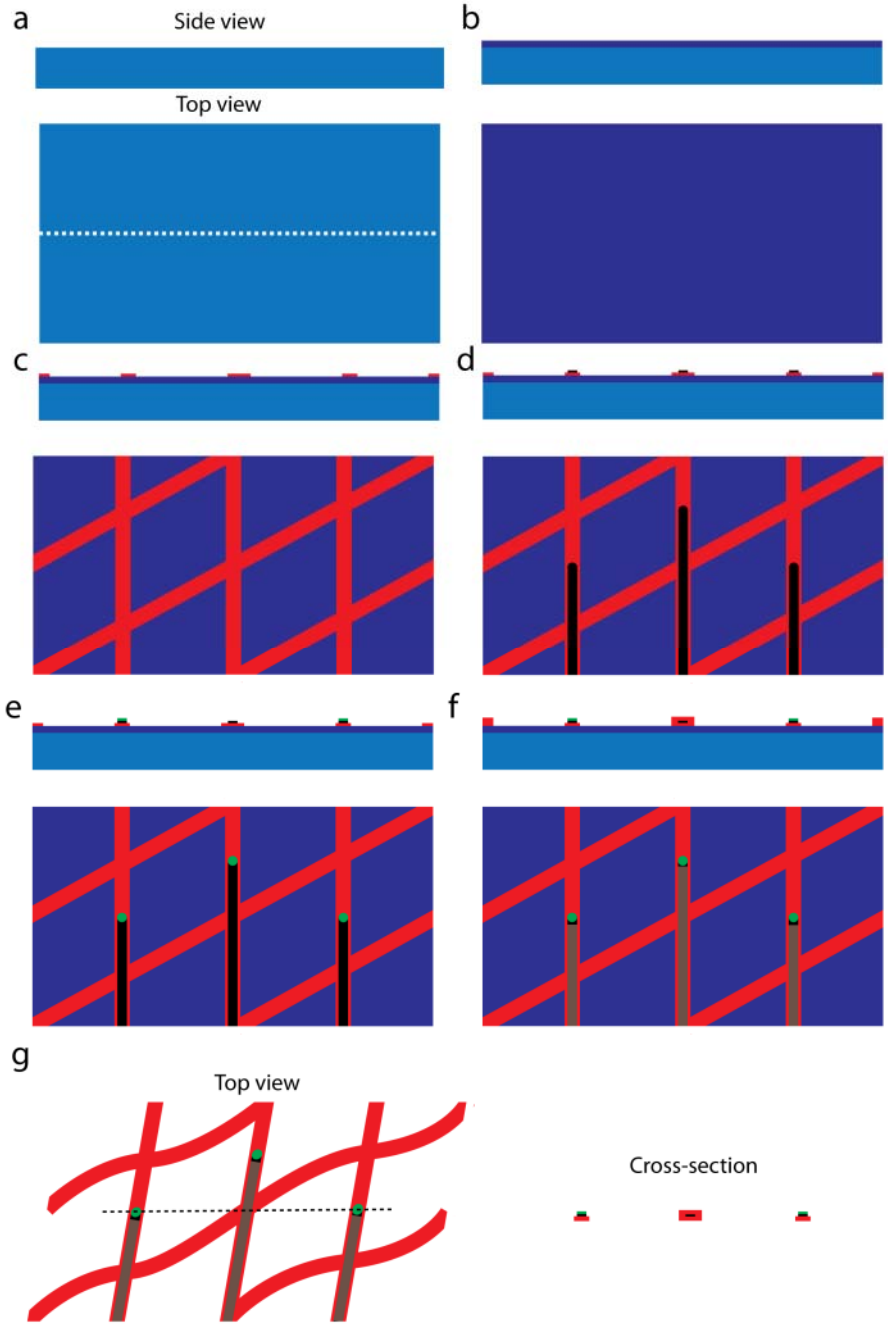

Supplementary Fig. 2. Schematics of mesh electronics fabrication. Components include silicon wafer (cyan), nickel relief layer (purple), SU-8 polymer ribbons (red), metal interconnects (black) and exposed metal electrodes (green). For each step a top-view and side-view are shown, where

the side-view corresponds to a cross-section taken at ca. the midpoint of top-view image and indicated by the dashed white line in **a**; the cross-section image (right panel) of **g** corresponds to the position of the black dashed line in the top view (left panel). The polymer ribbons defined by photolithography were 5-20 μm in width and 350-400 nm in thickness for each layer. The metal interconnects defined by thermal evaporator are Cr/Au, 2-10 μm in width and 5/100 nm in thickness. The exposed metal sensor electrode was Pt with 20 μm diameter and 50 nm thickness. Refer to **Materials and Methods** text for detailed description of the fabrication steps.

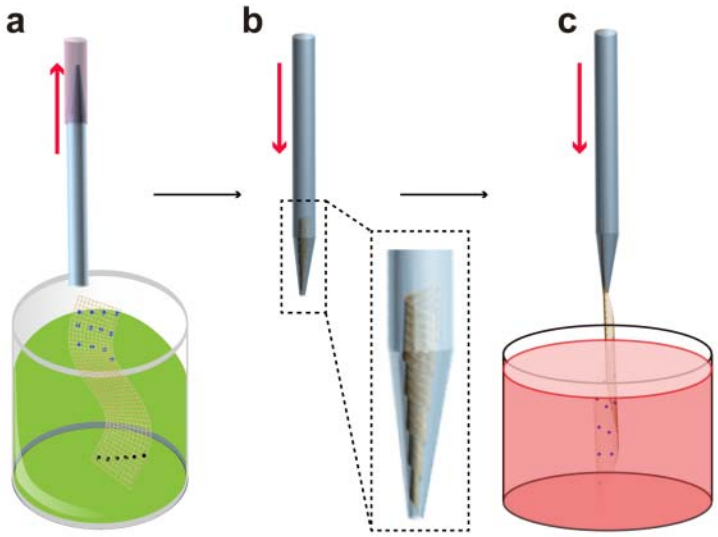

Supplementary Fig. 3. Loading and injection of mesh electronics. Schematics illustrating method used to load the mesh electronics into a glass needle and subsequently inject into a medium. **a**, The tip of the glass needle (blue) was connected to a syringe by a plastic tube (pink). The injectable mesh electronics (yellow) suspended in solution (green) was pulled into the needle from the large end of the glass needle such that the device end of the mesh enters the tube first. Black and blue dots represent the I/O pads and devices on the mesh electronics, respectively, where the two ends can be readily distinguished optically during the loading process. **b**, After the mesh electronics was loaded into the glass needle, the tubing was removed from the needle end and placed over the large end of the glass tube, and then the syringe was used to 'push' the mesh to the tip (inset, **b**). **c**, The glass needle was mounted in the x-y-z manipulator for injection into solution, gel/polymer or tissue (red). Red arrows indicate the direction of the fluid flow during loading and injection.

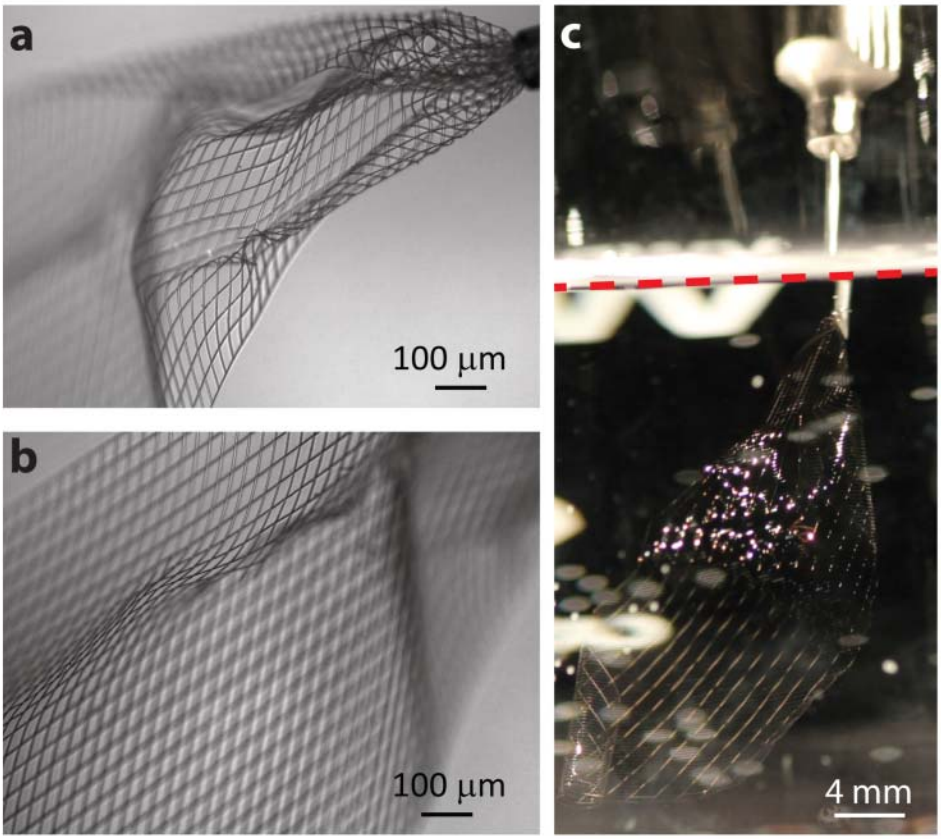

Supplementary Fig. 4. Injection of mesh electronics into aqueous solution. (**a** and **b**) Images showing the mesh electronics was injected into 1x PBS solution by a glass needle with ID of 95 μm corresponding to the 3D reconstructed fluorescence image in Fig. 1g. Bright-field microscopy images show the mesh electronics with limited unfolding structure near the needle region **a** corresponding to the blue dashed box highlighted region in Fig. 1g and completely unfolding structure **b** corresponding to the white dashed box highlighted region in Fig. 1g. **c**, Optical image of a 15 mm total width mesh electronics partially injected through a 20 gauge (ID = 600 μm) needle into 1x PBS solution. The device end of the mesh (lower-left to the middle of the image) is fully unfolded at this stage of injection with metal interconnect lines visible in the reflected light. The dashed red line corresponds to the air/solution interface, with the needle tip ca. 3 mm below the interface (upper-right of the image). The steps used for loading mesh electronics when injecting through metal needles are as follows: (1) The suspended mesh electronics was loaded into a glass pipette starting from the I/O end; (2) The mesh electronics

was then transferred to the syringe from plunger side with device region close to the needle/syringe connection and the mesh extended in the longitudinal (injection) direction. At this point, the mesh electronics could be injected into the desired medium or structure through the metal needle. The mesh electronic structural properties are summarized in Supplementary Table 1, entry-1.

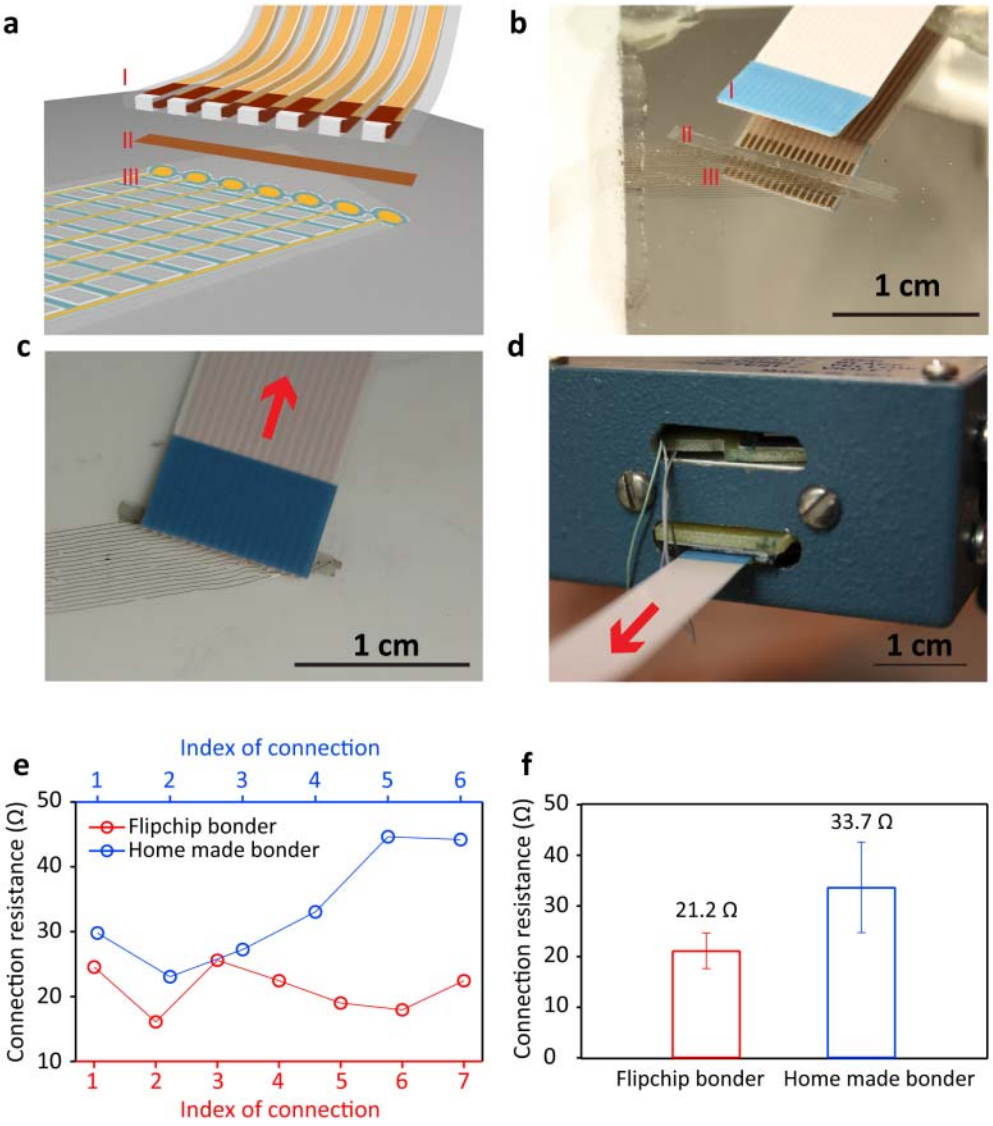

Supplementary Fig. 5. Flexible cable to I/O bonding. Schematic **a** and corresponding photograph **b** of the overall process of bonding a flexible cable to the I/O pads of the mesh electronics. In both the schematic and photograph, the flexible cable, anisotropic conductive film (ACF) and I/O region of the mesh electronics are indicated by **I**, **II** and **III**, respectively. **c**, Photograph shows the flexible cable bonded to the I/O pads of the mesh electronics. The red arrow indicates the direction of flexible cable connection to the external hardware. **d**, Photograph shows another end of the flexible cable connected to the amplifier for electrical recording. Red arrow indicates the direction of flexible cable connection to the I/O pads. **e**, Connection resistance of the cable/ACF/mesh bonded by a commercial flip-chip bonder (red) and home-

made bonder (blue). **f**, Histogram summary of the connection resistance data in **c** showing the average value ±1 standard deviation (1SD).

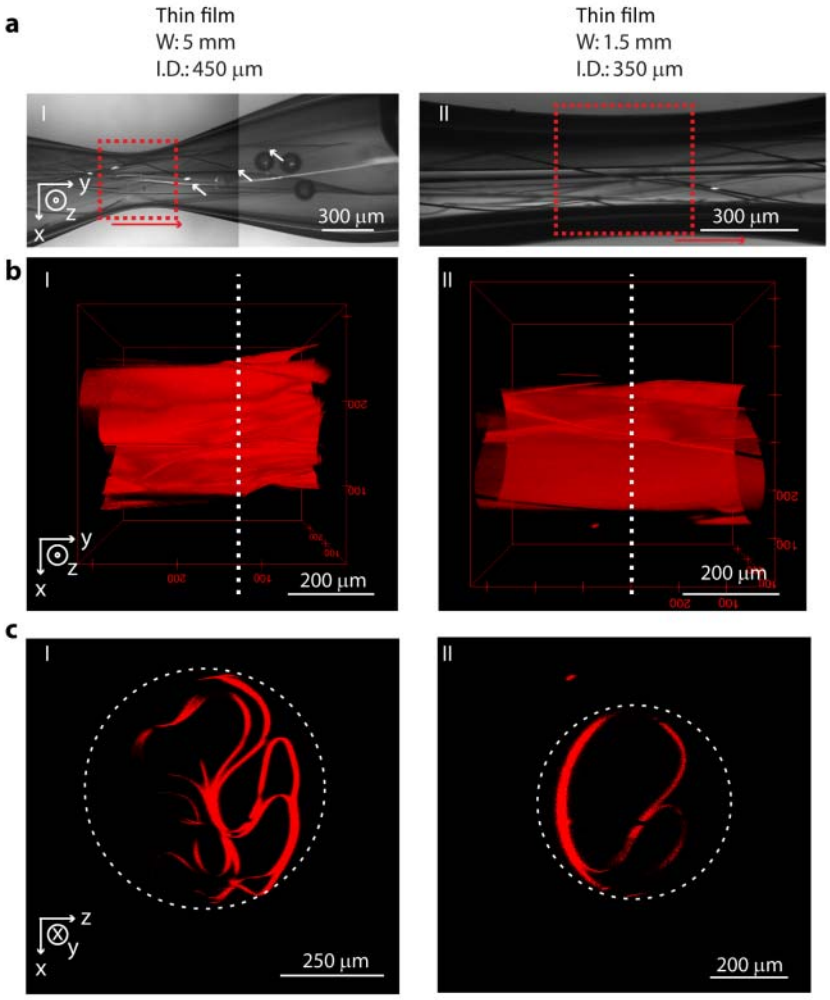

Supplementary Fig. 6. Injection of thin film electronics into needle-like constrictions. **a**, Bright-field microscopy image of an attempted injection of a 5 mm total width thin film electronics sample through a 400 μm ID glass channel **I**, and a 1.5 mm wide thin film electronics being injected through a 350 μm glass channel **II**. Red arrows indicate the direction of injection. The continuous thin films have the same polymer and metal thicknesses as the mesh electronics. White arrows in **I** indicate the ends of metal lines where the thin film 'jams' and cannot pass through the needle. **b**, 3D reconstructed confocal fluorescence microscopy images recorded from the regions in **a** highlighted by the dashed red boxes. **c**, Cross-sections of through images in **b** at the positions of the vertical white dashed lines. The white dashed circles in **c** indicate the approximate IDs of the glass constrictions. The coordinate axes for images are shown in **I** of (**a** to **c**) and refer to the schematic for imaging in Fig. 2a. They are the same for **II**.

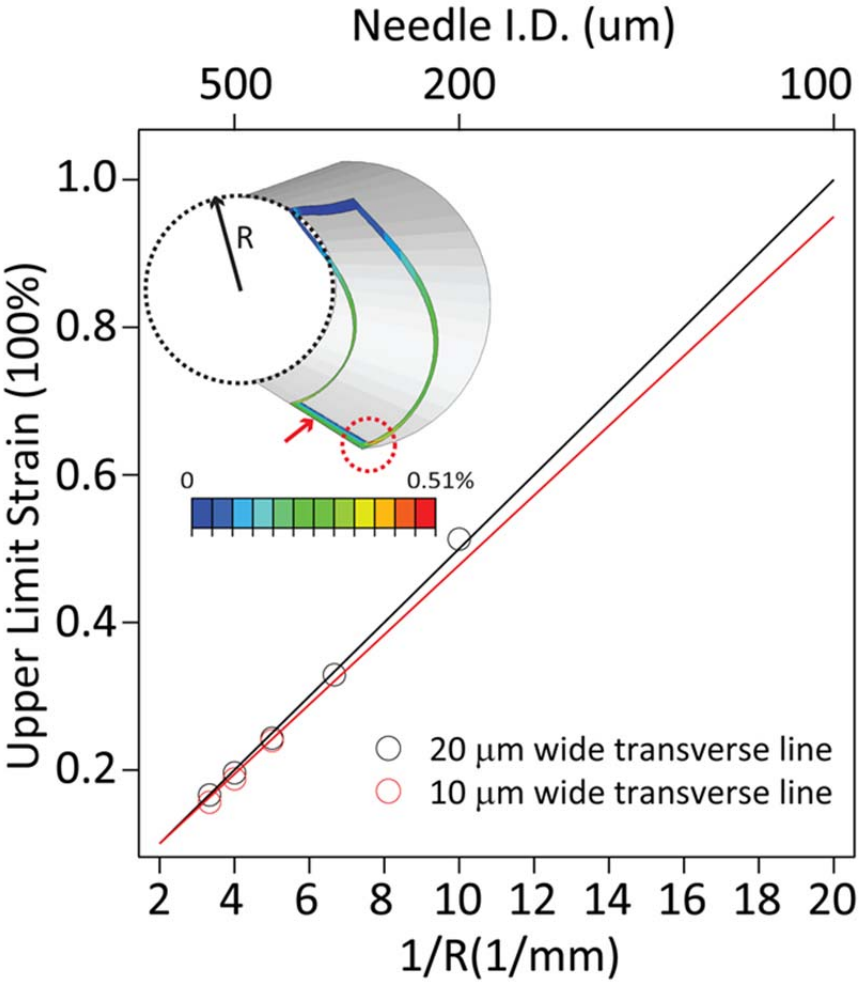

Supplementary Fig. 7. Calculated mesh electronics strain versus needle size. Plot of the upper bound for the strain of the mesh as a function of the inverse needle radius, 1/*R*. Simulations were made for single unit cell. The black and red circles represent meshes with 20 and 10 μm width transverse ribbons, respectively. The black and red lines correspond to linear fits to the respective simulation points. The inset is a representative simulation shows the strain distribution of one unit cell in a 200 μm ID needle. The red dashed circle highlights the point with highest maximum principle strain. Black dashed circle and black arrow show the inner boundary and radius of the needle, respectively.

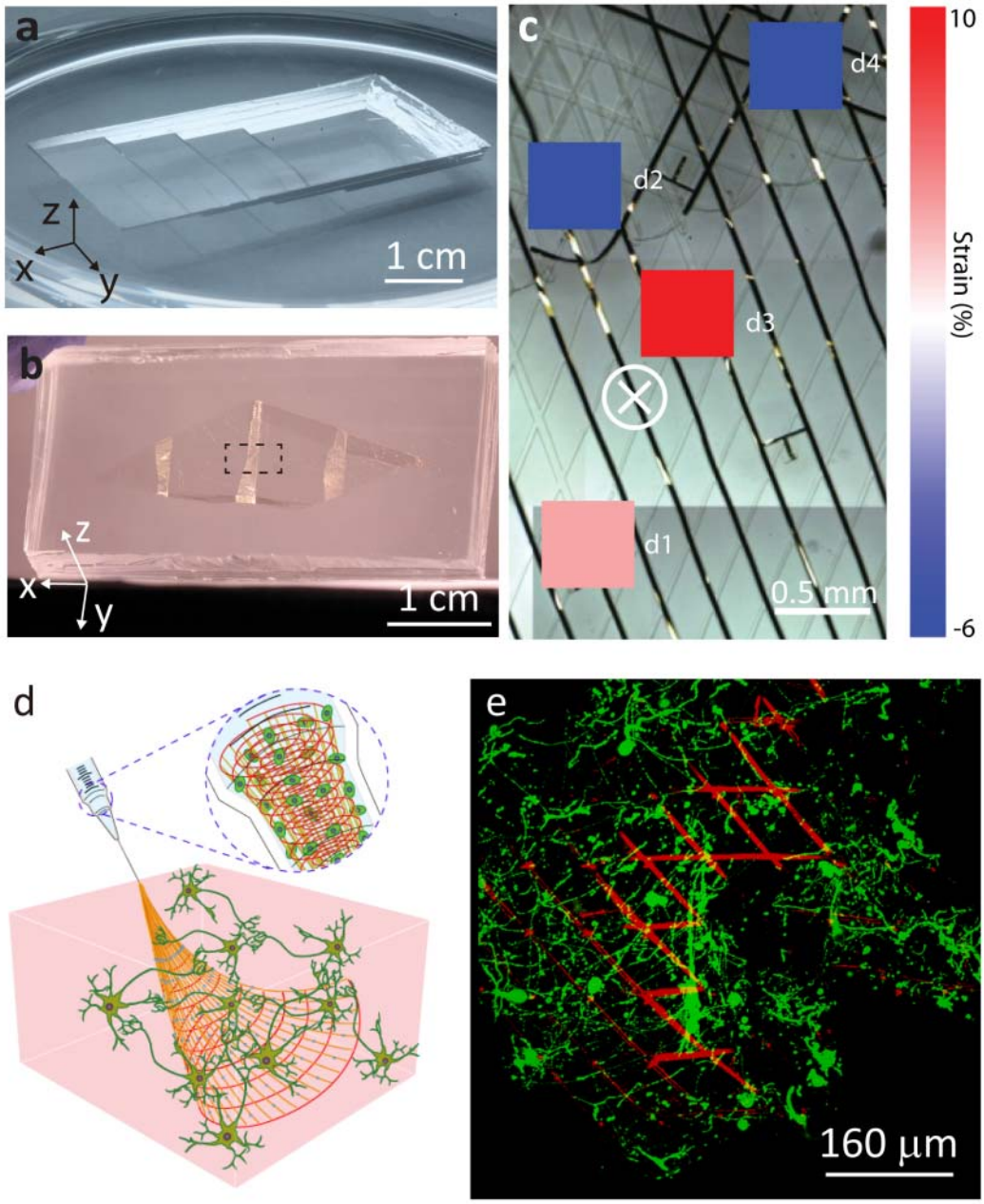

Supplementary Fig. 8. Injection of mesh electronics into 3D cavities and gels. **a**, Photograph of a typical polydimethylsiloxane (PDMS) cavity before injection, where the cavity has a stepped internal structure. **b**, shows the hybrid structure of a mesh electronics embedded in a similar PDMS internal cavity after injection. The black dashed box highlights the region where the

micro-computed tomography (μCT) image shown in Fig. 3b was recorded. **c**, Image of the mesh electronics injected and unfolded within a PDMS cavity. The positions of the four nanowire sensors are indicated by d1, d2, d3 and d4. The strain field was applied to the PDMS/mesh electronics hybrid at the position indicated by white vector arrow. The strain field was color mapped (relative to the point force was applied) for the nanowire strain sensors using the calibration of the nanowire devices corresponding to the data in Figure 3c. The detected strains are labeled in the PDMS/mesh electronics microscopic image at the device positions. **d**, Schematic of the co-injection of mesh electronics with cells. The red lines highlight the overall mesh structure and indicate the region of supporting and passivating polymers and the yellow lines indicate the metal interconnects for the devices (blue filled circles). Green spheres highlight the structure of cells co-injected with mesh electronics. **e**, Projection of 3D reconstructed confocal image from 100 μm thick, 635 μm long and 635 μm wide volume shows the interpenetration between neurons and mesh structure of injectable electronics after co-injected into Matrigel for 14 days. The red and green colors in this correspond to SU-8 and β-tubulin, respectively.

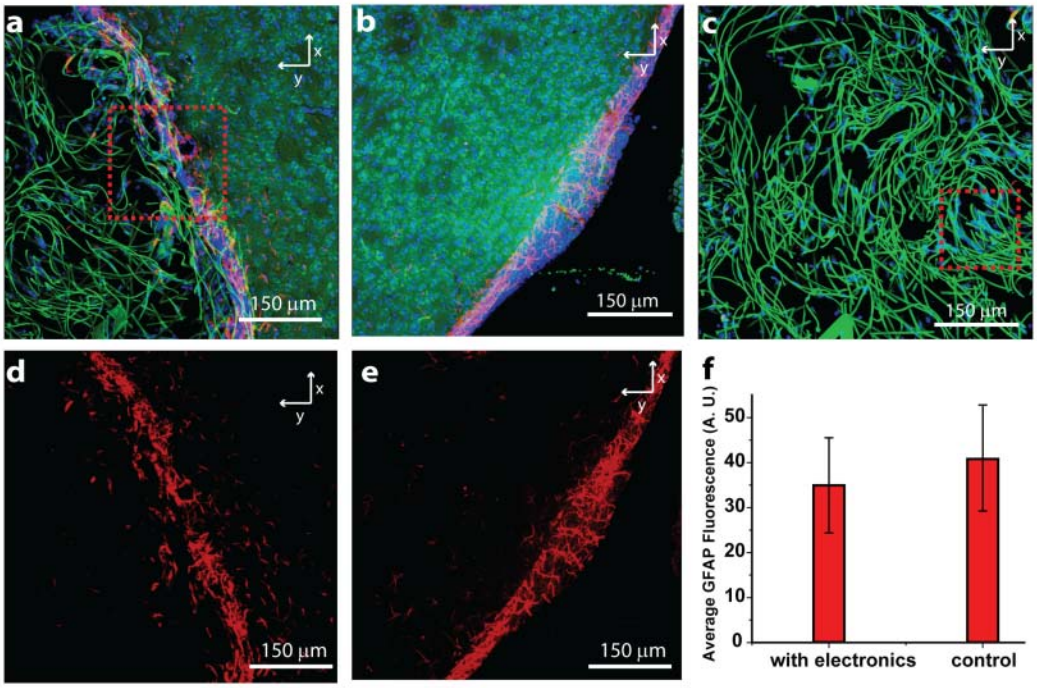

Supplementary Fig. 9. Chronic histology of interface between mesh electronics and subventricular zone of mouse brain. Mesh electronics were injected into the LV as shown schematically in Fig. 4c and the animals were returned to the animal facility. Five weeks (post injection) mice were euthanized and their brain tissue was fixed and sliced for staining and imaging. **a**, Projection of 3D reconstructed confocal image from 30 µm thick, 635 µm long and 635 µm wide volume at the region indicated by the dashed white box in Fig. 4e. The dashed red box corresponds to the higher-resolution image shown in Fig. 4f. In this and following images: blue corresponds to DAPI staining of cell nuclei, green represents SU-8 ribbons and NeuN staining of neurons and red highlights GFAP staining of astrocytes. **b**, Control image recorded from the LV of the opposite hemisphere without injected mesh electronics. The tissue slice was the same as used to obtain data panels **a** and **c**. **c**, Projection of 3D reconstructed confocal microscopy image 80 µm thick, 635 µm long and 635 µm wide volume for the region highlighted by the white box in Fig. 4e. The dashed red box indicates the higher-resolution image shown in Fig. 4g. **d** and **e**, GFAP fluorescence channels from **a** and **b**, respectively. **f**, the integral of fluorescence intensity (mean ± 1SD) along the interface between the electronics and subventricular region (**d**) was analyzed and compared with that in control sample (**e**). The fluorescence intensity was averaged and analyzed for 20x20 µm regions (n=10) along the interface between mesh electronics/subventricular zone and the natural boundary of subventricular zone in the control sample.

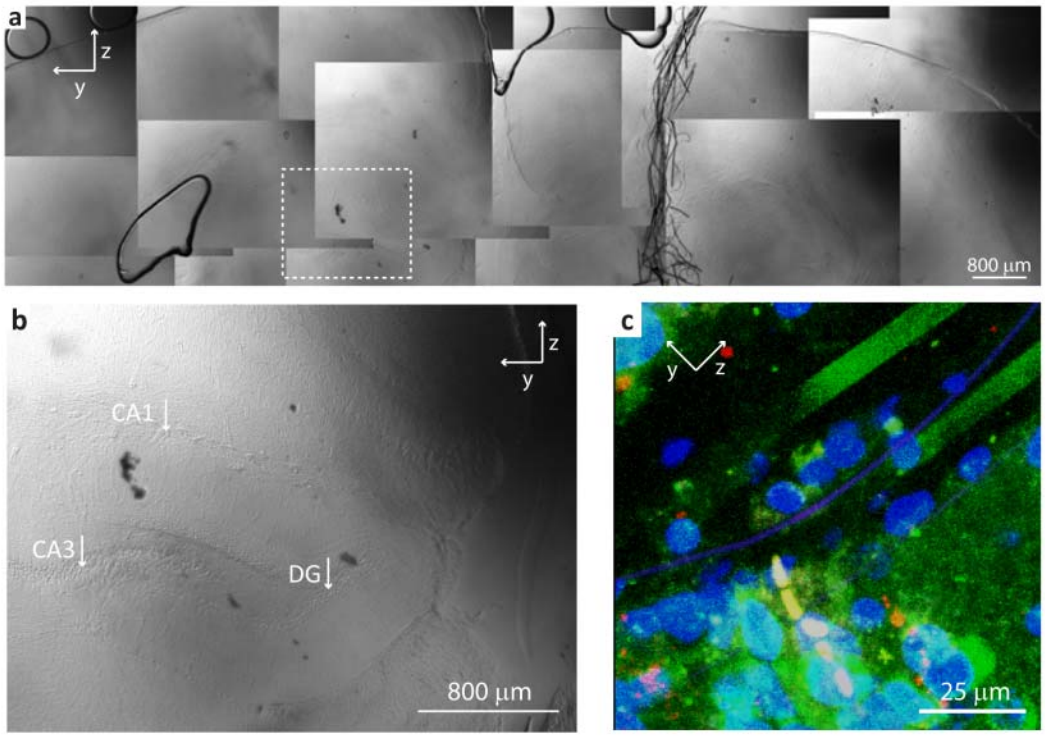

Supplementary Fig. 10. Chronic imaging of mesh electronics injected into the hippocampus. **a**, Composite bright field image of a mesh electronics injected through the mouse cortex into the HIP. The mesh electronics was fully extended along the injection/longitudinal direction and partially unfolded in the transverse direction. Black dashed lines indicate the boundary of each image. **b**, Image from the white dashed box in **a** shows the HIP region of the hemisphere opposite to the hemisphere where the injection was carried out. **c**, Projection of 3D reconstructed confocal microscopy image from dashed red box in Fig. 4j. Mice were euthanized 5 weeks post injection, and then brain tissue was fixed and sliced for staining and imaging.

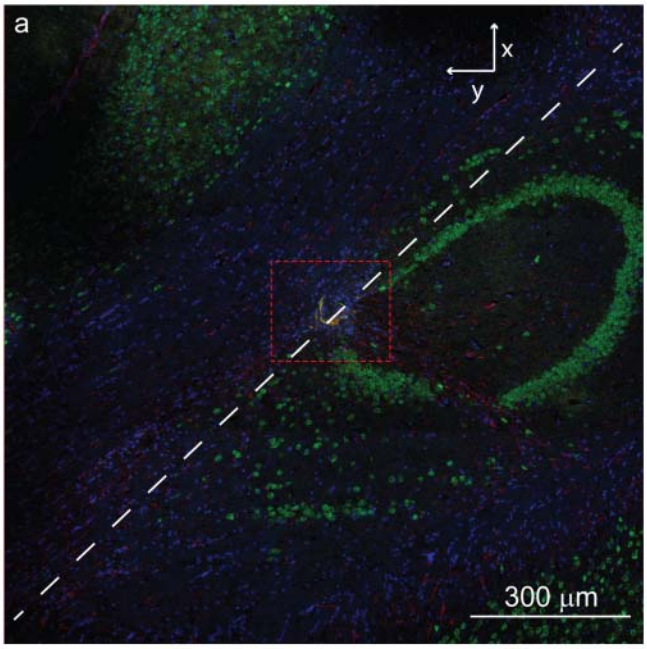
a
x
y
300 μm

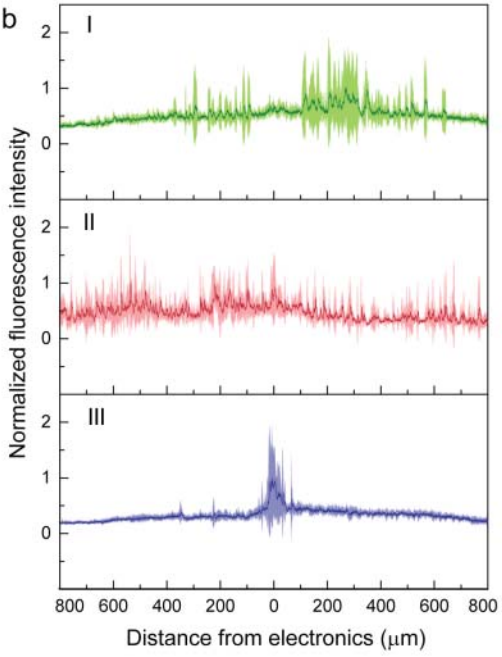
b
I
II
III
Normalized fluorescence intensity
2
1
0
800 600 400 200 0 200 400 600 800
Distance from electronics (μm)

Supplementary Fig. 11. Chronic histology of the interface between mesh electronics and the hippocampal region of a mouse brain. **a,** Projection of a 3D reconstructed confocal image from 10 μm thick, 1.2 mm long and 1.2 mm wide volume at the region indicated by the dashed blue line in Fig. 4d. The dashed red box indicates the position of the injected mesh electronics. Blue corresponds to DAPI staining of cell nuclei, yellow represents SU-8 ribbons, green represents NeuN staining of neurons and red highlights GFAP staining of astrocytes. White dashed line highlight the region and direction where the fluorescence signals were averaged and analyzed for comparison of NeuN, GFAP and SU-8 signal intensities. **b**, Fluorescence intensity plotted corresponding to the region in a, where fluorescence intensity in each channel in 70 μm × 1600 μm area was averaged and normalized. **I**, **II** and **III** corresponds to signals from NeuN, GFAP and SU-8 channels, respectively. Solid lines and shaded areas represent average intensities and s.e.m. values, respectively. The normalized factors are 47 for NeuN signal, 27 for GFAP signal and 48 for SU-8 signals (i.e., the NueN and SU-8 raw signals are ca. 2x larger than the GFAP signal).

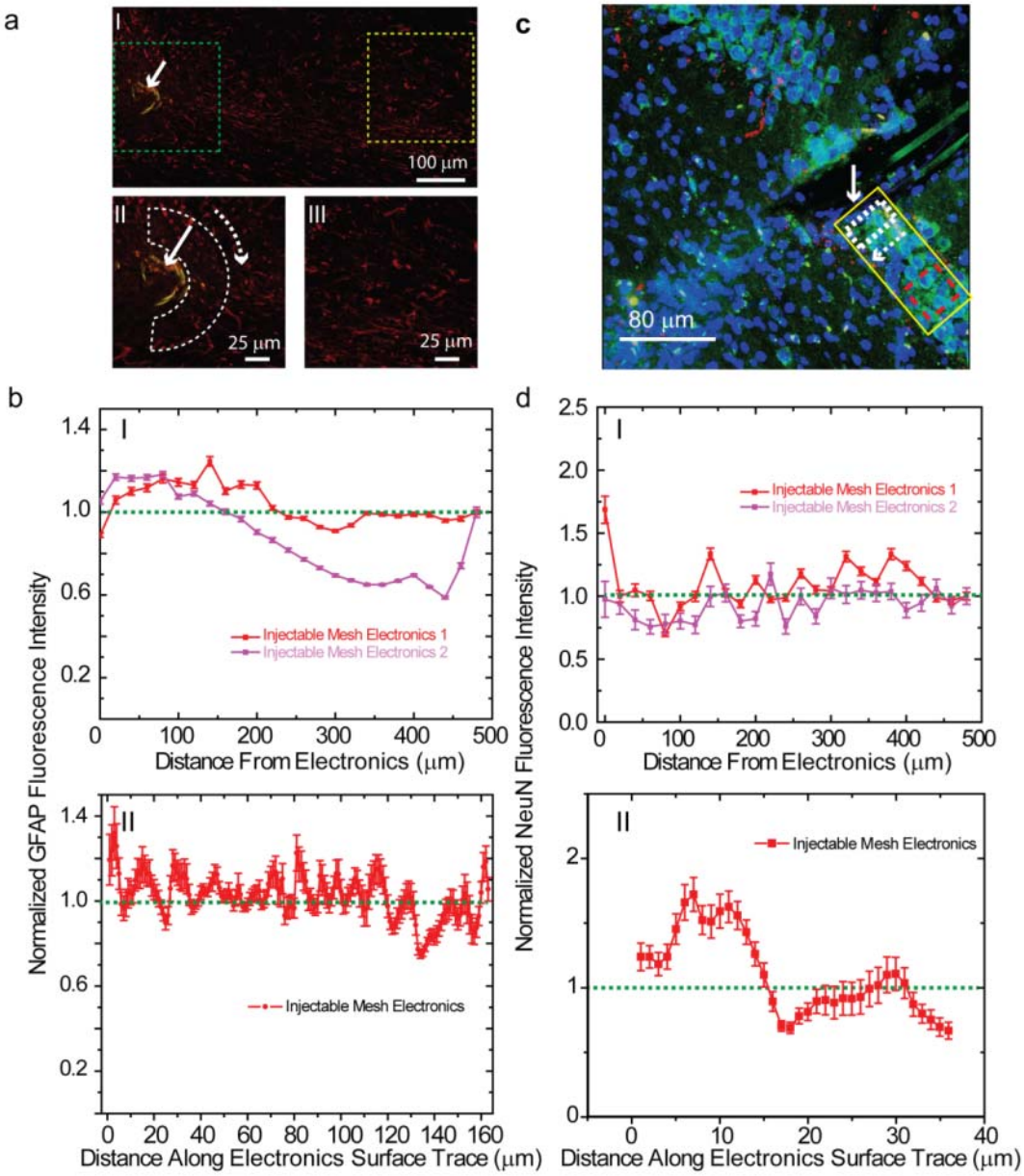

Supplementary Fig. 12. GFAP and NeuN density vs. distance from and along implanted mesh electronics. **a**, Confocal microscopy fluorescence images of GFAP from injectable mesh electronics-1 sample. Red and yellow colors correspond to GFAP and SU-8 structures from mesh electronics, respectively. Solid white arrows highlight the ribbons from mesh electronics. II and III are zoomed-in higher resolution images corresponding to the green and yellow dashed boxes, respectively, in I. **b, I**, GFAP fluorescence intensities and standard error of the mean (s.e.m.) 4 weeks post implantation versus distance from the interface of two different injected mesh electronics samples. The fluorescence intensity was normalized with the background value for each sample (value = 1, green dashed line) for comparison. **b, II**, Normalized fluorescence intensity of GFAP (red points/line) and s.e.m. plotted along the outer curved surface of the mesh

electronics highlighted by the white dashed box in II; the normalized background fluorescence intensity level was determined from III (480 μm away from the electronics surface). The direction of GFAP plot is top to bottom along the curved surface (white dashed arrow in II). **c**, Confocal fluorescence image of mesh electronics injected into the hippocampus (Fig. 4j, manuscript), where blue, green and red correspond to nuclei, NeuN and SU-8 auto-fluorescence, and GFAP. The yellow box highlights the neuron region analyzed in **d, II**. NeuN fluorescence intensity and s.e.m. 4 weeks post implantation versus distance from the interface of two different injected mesh electronics samples. Fluorescence intensity was normalized to the background value for each sample, where normalized background has value of 1. **d, II**, Normalized fluorescence intensity and s.e.m. of NeuN plotted along the probe surface highlighted by the white dashed box in **c**, and the normalized background fluorescence intensity level (black dashed line, value = 1) from red dashed box in c. The white dashed arrow in c highlights the direction of plots in d, II. The red box/background region in c represents a higher background than that obtained from averaging the entire image, and thus yields a lower limit on enhanced normalized NeuN signal at the injected mesh probe surface. All the data were analyzed by Matlab.

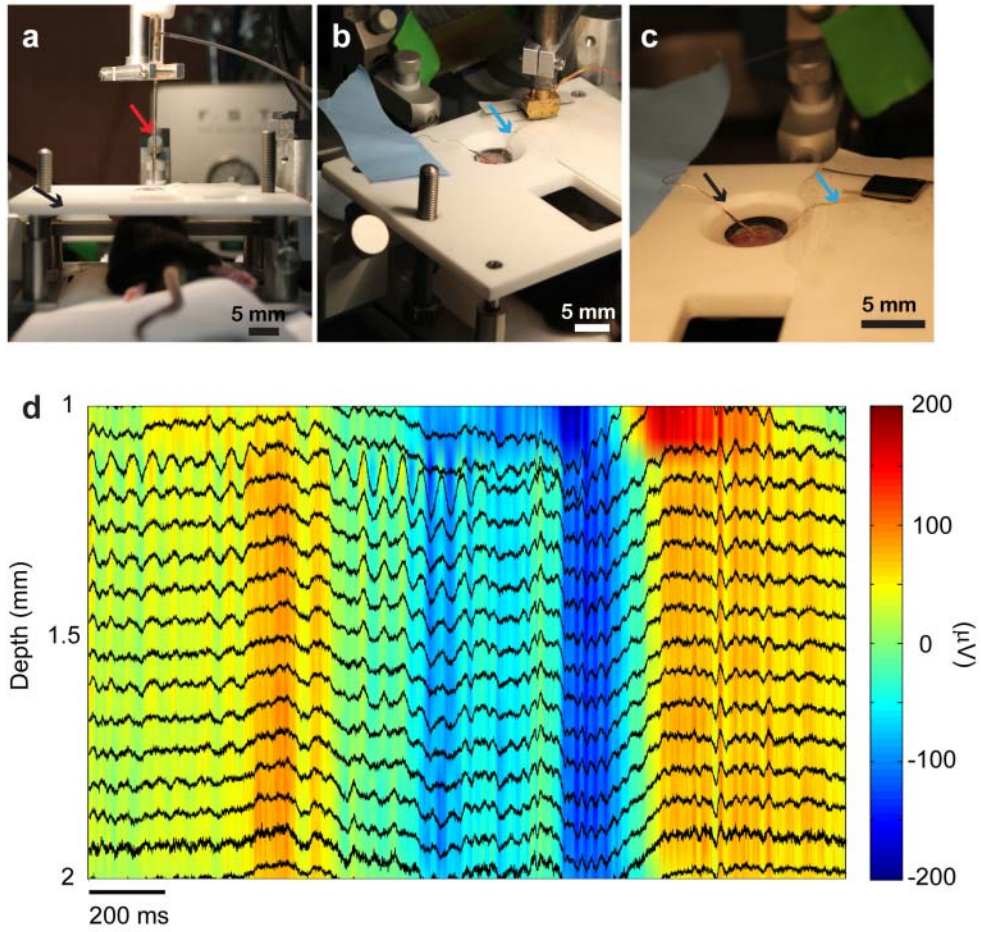

Supplementary Fig. 13. Acute *in vivo* recording with mesh electronics. **a**, The mouse was fixed in the stereotaxic frame, its skin was retracted and a hole was drilled through the skull plate and a ceramic scaffold (black arrow) was placed on top of the mouse skull with opened centered over the hole in the skull. The mesh electronics was injected into the mouse brain through a glass needle, where the red arrow indicates the position of the glass needle. **b**, A flexible flat cable was bonded to the mesh I/O pads, where the blue arrow indicates the unfolded I/O region of the mesh electronics. **c**, Electrophysiological recording, where black and blue arrows indicate Ag/AgCl reference electrode and unfolded I/O region of the mesh electronics, respectively. **d,** Map of the acute *in vivo* mouse brain recordings from the region in Fig. 4k highlighted by the dashed red box. The y-axis represents the depth beneath the brain surface of each sensor electrode whose spatial distribution is shown in Fig. 4k. The x-axis shows the recording time. Colors indicate the amplitude of the recorded LFP amplitudes.